Bulk photovoltaic effect of a hybrid ferroelectric semiconductor

Yunlin Lei [iD],[1] Wei Hao [iD],[1,2] Shouyu Wang [iD],[3,*] Yinxin Bai,[1] Chuanshou Wang [iD],[1] Junjiang Tian,[1] Li Huang [iD],[1] Xiaoting Ma,[3] and Junling Wang[1,†]

[1]*Department of Physics & Guangdong Provincial Key Laboratory of Functional Oxide Materials and Devices, Southern University of Science and Technology, Shenzhen 518055, Guangdong, China*

[2]*MOE Key Laboratory of Macromolecular Synthesis and Functionalization, International Research Center for X Polymers, Department of Polymer Science and Engineering, Zhejiang University, Hangzhou 310027, China*

[3]*College of Physics and Materials Science, Tianjin Normal University, Tianjin 300387, China*

Hybrid ferroelectrics have attracted much attention recently due to their low processing cost and superior piezoelectric responses. However, their photovoltaic properties are less explored. For better performance, ferroelectric semiconductors with small band gaps are desired. Here, we report on an organic-inorganic hybrid material (MV) [SbI$_5$] (MV^{2+} = N, N′-dimethyl-4,4′-bipyridinium or methylviologen), with a band gap of 1.47 eV, which exhibits ferroelectricity at room temperature. Careful analysis shows that a flat band formed by the MV not only enhances light absorption but also allows for the simultaneous manifestation of small band gap and ferroelectricity in the same material. Under the irradiation of a 445 nm laser, we observed an open circuit voltage of ∼5 V, far greater than its band gap. The light polarization-dependent photocurrent confirms that the above-band-gap photovoltage is caused by the bulk photovoltaic effect (BPVE). Further investigations revealed that the contribution of the MV group to the conduction band leads to two distinct electron excitation pathways for (MV) [SbI$_5$] under visible and infrared light illumination, resulting in photocurrents in opposite directions. In this paper, we offer a strategy for designing hybrid ferroelectrics with narrow band gaps and improve our understanding of the BPVE.

I. INTRODUCTION

Photovoltaic devices capable of converting light into electricity are widely used for energy harvesting and photodetection. The process involves the absorption of light, the creation of electron-hole pairs, and the separation of them under some form of build-in asymmetry [1]. In conventional photovoltaic devices based on *p-n* junctions and metal-semiconductor heterojunctions, the electron-hole pair separation is done by the built-in electric fields at the interfaces [2]. The technology is rather mature, and the energy conversion efficiency is coming close to the Shockley-Queisser limit [3]. For example, efficiency of solar cells based on the recently developed hybrid lead halide perovskites (represented by the MAPbI$_3$) has exceeded 25% after only ∼10 years [4], even though the mechanism behind their long carrier lifetime and diffusion length remains controversial [5,6]. Part of the controversy centers around the effect of spontaneous polarization in these materials. Since both nonpolar *I4/mcm* and polar *I4cm* space groups are possible for MAPbI$_3$ at room temperature, the contribution of these two phases to the high conversion efficiency of the device is still uncertain [7–10].

Recently, much renewed interest has been dedicated to the bulk photovoltaic effects (BPVEs) of ferroelectric materials [11–14]. Their inherent spontaneous polarization is considered helpful for charge separation and facilitating carrier transport. More importantly, the BPVE offers a totally different mechanism for separating the photogenerated electron-hole pairs, which is not limited by the band gap of the photoactive materials [15]. Furthermore, the possibility of switching the polarization via external electric fields enables the switchable photovoltaic effect, which may find applications in sensors and memory devices [16,17]. Previous studies on the BPVE have focused mostly on conventional oxide ferroelectrics such as BiFeO$_3$ and BaTiO$_3$ [15,18–20]. However, their band gaps are usually >2.5 eV, limiting the amount of sunlight that can be absorbed. Inspired by MAPbI$_3$, the field has seen a wave of research into hybrid ferroelectric semiconductors recently. Many hybrid ferroelectrics with smaller band gaps have been reported, e.g., hexane-1,6-diammonium pentaiodobismuth (HDA-BiI$_5$, E_g: 1.89 eV) [21], (isopentyl-ammonium)$_2$(ethylammonium)$_2$Pb$_3$I$_{10}$ (PEPI, E_g: 1.8 eV) [16], (BA)$_2$(EA)$_2$Pb$_3$I$_{10}$ (BA = n-butylammonium and EA = ethylammonium, E_g: 1.9 eV) [22], and (4, 4−DFPD)$_2$PbI$_4$ (4,4-DFPD is 4,4-difluoropiperidinium, E_g: 2.24 eV) [23]. Note that these small-band-gap hybrid ferroelectrics are mostly realized by replacing the halogen element in the inorganic frameworks with iodine or increasing the thickness of the inorganic sheets in the two-dimensional lattice, which is consistent with the fact that their band-edge states are dominated by the metal-halide framework [24–26].

In general, the organic cations are thought only to deform the metal-halide framework structurally and affect the valance band and conduction band indirectly [27]. However,

---
*sywang@mail.tjnu.edu.cn

†jwang@sustech.edu.cn

recent studies have demonstrated that conjugated organic cations contribute to the band-edge structures of hybrid materials [28], which opens possibilities in synthesizing hybrid ferroelectrics with small band gaps. Inspired by the recent reports on hybrid ferroelectrics containing π-conjugated organic cations [29,30], we present a hybrid ferroelectric (MV) [SbI$_5$] (MV^{2+} = N, N$'$-dimethyl-4,4$'$-bipyridinium or methylviologen) with a band gap of 1.47 eV and a spontaneous polarization of $\sim$4 μC/cm^2. Careful analysis shows that the distortion of the SbI$_6$ octahedron caused by the nonpolar MV groups leads to the polarization of (MV) [SbI$_5$]. Furthermore, the flat band formed by the MV groups not only enhances light absorption but also allows for the simultaneous manifestation of a small band gap and ferroelectricity in the same material. Interestingly, under light excitation, electron transitions from the valence band maximum (VBM) dominated by the [SbI$_5$] chains to the flat band contributed by the MV groups or the higher band determined by the [SbI$_5$] chains result in photogenerated currents with completely opposite directions. This phenomenon is attributed to changes in the spatial shift vectors of electrons upon excitation to different states, as elucidated by first-principles calculations.

II. EXPERIMENTAL METHODS

A. Materials

All the chemicals, antimony iodide (SbI$_3$, Bidepharmatech), 4,4$'$-bipyridine (Mreda), hydroiodic acid (HI, 48%, Innochem), methanol (MeOH, Xilong scientific), were bought and used without further purification.

B. Synthesis

The hybrid ferroelectric (MV) [SbI$_5$] was synthesized by using the solvothermal reaction method with a bipyridine radical cation molecular and metal halide compound. Firstly, 0.12 g of SbI$_3$, 2 mL of HI (48%), 0.044 g of 4,4$'$-bipyridine, and 10 mL MeOH were mixed in a 25 mL Teflon bomb. The Teflon bomb was then sealed in a Parr autoclave and heated in a programmable oven with the following parameters: heating from 25 °C to designated temperature of 185 °C, holding at 185 °C for 48 h, and then cooling to 25 °C with 2 °C/h. The black rod-type crystals were obtained.

C. Single-crystal and powder x-ray diffractions

Variable-temperature single-crystal diffraction data of (MV) [SbI$_5$] were collected on a Rigaku XtalAB PRO MM007DW diffractometer with Mo-$K\alpha$ radiation (λ = 0.77 Å) at 80 K and room temperature, respectively. Powder x-ray diffraction (PXRD) for (MV) [SbI$_5$] was performed on a Rigaku D-max 2500 PC for Cu $K\alpha$ radiation at room temperature.

D. Ultraviolet-visible-near-infrared absorption spectra

Ultraviolet-visible-near-infrared (UV-vis-NIR) absorption spectra measurement was performed at room temperature using a UV-3600 UV-vis-NIR spectrophotometer.

E. Thermal measurements

Differential scanning calorimetry (DSC) measurement was performed using the NETZSCH DSC 200F3 with heating/cooling rates of 3 K/min.

F. Electrical measurements

For ferroelectric measurement, conductive silver paste was used as the electrode, which had a circular shape and was deposited onto the surface perpendicular to the b axis of the plate-shaped crystal. The effective area of the electrode was 0.8 mm^3, while the distance between electrodes (i.e., the thickness of the plate-shaped crystal) was $\sim$0.5 mm. An aixACCT TF-2000 analyzer operating at a frequency of 10 Hz with a triangular wave in the virtual ground mode was used to measure the polarization-electric field (*P-E*) hysteresis loop and current-electric field loop. Photoelectric measurements were performed with parallel electrode configurations. The light source consisted of a power-adjustable 445 nm laser (CHIlaser MDL-III-445–200 mW, Changchun New Industries Optoelectronics Tech. Co., Ltd, China) and laser diodes (KYD405NX-T1685, KYD450N100-T1685, KYD520N100-G2290, and D650NX-T1685, Shenzhen Jukun Optical Technology Co., Ltd, China. ZL808AD100-GD16; and ZL905AD200-GD16, and ZL950AD750-FGD16, Shenzhen Zhonglai Technology Co., Ltd, China) emitting light at wavelengths of 405, 450, 520, 650, 808, 905, and 950 nm, respectively. The photovoltaic response under different laser illuminations were measured using Keithley 2636B. The polarization-dependent photocurrents were also carried out using a Keithley 2636B source meter.

G. Calculations of electronic structure

The first-principles calculations were performed for the single-crystal structure data of (MV) [SbI$_5$] based on the density function theory (DFT) within VASP [31,32]. The projector augmented-wave method was used to describe the electron-ion interaction [33], and the exchange-correlation between electrons was described by the hybrid functional in the form of HSE06 [34]. The energy cutoff of the plane-wave basis was set to 500 eV, and the numerical integration of the Brillouin zone was performed using a Monkhorst-Pack k-point sampling of 4 × 2 × 2. Our optimized latter parameters for (MV) [SbI$_5$] in the ferroelectricity phase were $a = 6.579$ Å, $b = 15.014$Å, $c = 11.081$Å, and $\beta = 102.46°$, which agree well with our experimental data of $a = 6.488$Å, $b = 14.886$Å, $c = 11.466$Å, and $\beta = 101.94°$.

III. RESULTS

A. Preparation of (MV) [SbI$_5$] single crystals, structural analysis, and ferroelectric property characterizations

The crystal structure of (MV) [SbI$_5$] is schematically shown in Fig. 1(a). Bulk single crystals as large as 18 × 0.8 × 0.3 mm^3 (Fig. S1(a) in the Supplemental Material [35]) were prepared by solvothermal method from the methanol solutions containing 4,4$'$-bipyridine and SbI$_3$ of the stoichiometric molar ratio. Atomic force microscopy images
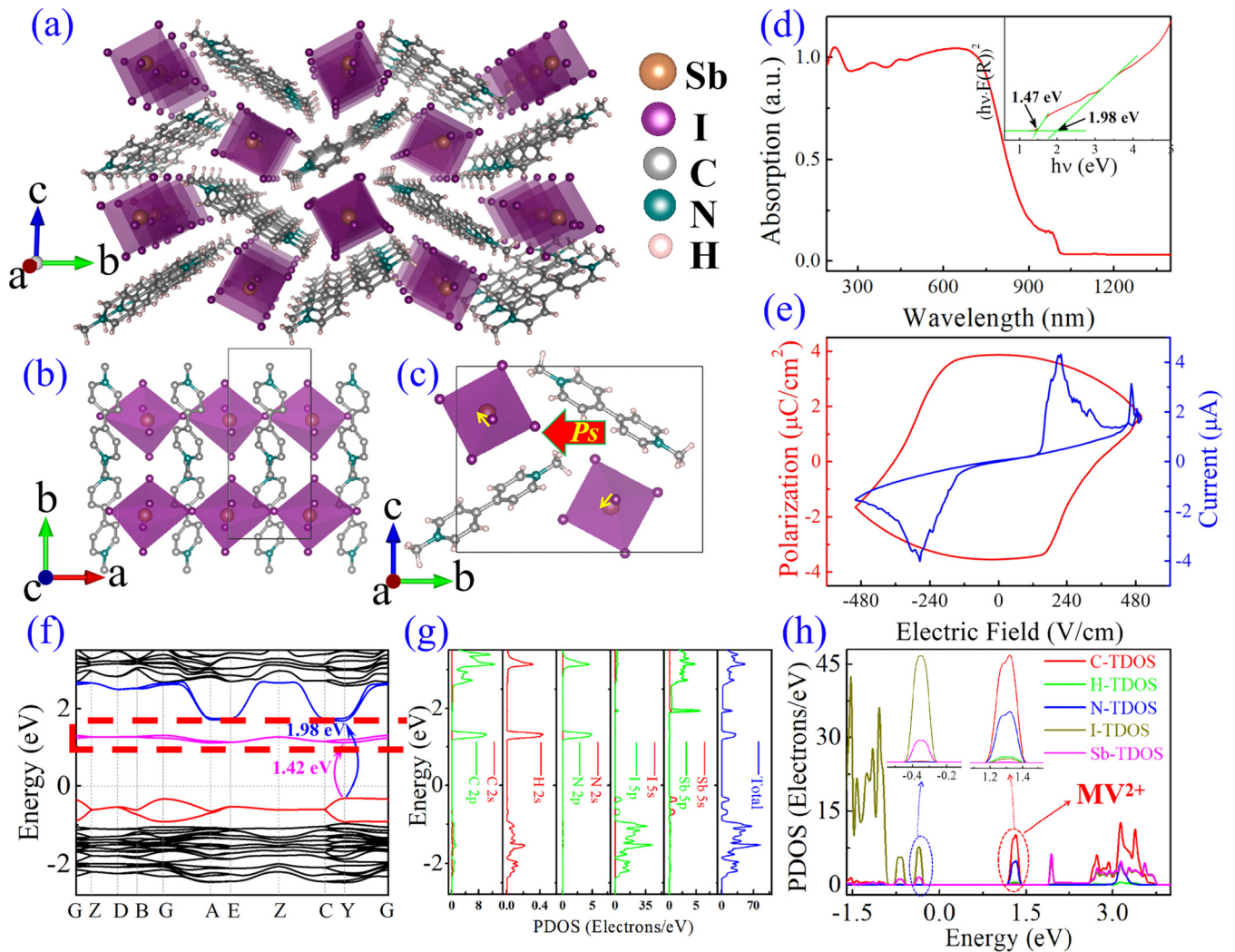
FIG. 1. (a) and (b) Crystallographic structures of (MV) [SbI$_5$] along the one-dimensional (1D) chain (a) and c directions, respectively. (c) Origin of spontaneous polarization in (MV) [SbI$_5$]. (d) The absorption spectrum of (MV) [SbI$_5$]. (e) P-E hysteresis loop and I-V curve of (MV) [SbI$_5$] measured along the b axis at room temperature. (f) Energy band structure. (g) Partial density of states (PDOS) of (MV) [SbI$_5$]. (h) Density of states (DOS); inset: zoomed-in DOS.

(Fig. S1(b) in the Supplemental Material [35]) reveal atomically flat surface for the as-grown crystals. PXRD was used to confirm phase purity (Fig. S2 in the Supplemental Material [35]). DSC measurements show exothermic and endothermic peaks during cooling and heating (Fig. S3(a) in the Supplemental Material [35]), indicating reversible phase transitions. We label the three phases of (MV) [SbI$_5$] as α phase (<121 K), β phase (121–556 K), and high-temperature phase (HTP, 556–574 K).

Better understanding of the phase transition in (MV) [SbI$_5$] was achieved through analyzing the crystal structures (for crystal data, see Table S1) by single-crystal XRD at various temperatures. It is shown that the β phase belongs to the monoclinic system with a polar space group of $P2_1$. The inorganic $\{SbI_5\}_n$ chains are packed along the a axis to generate the one-dimensional framework [Fig. 1(a)], within which the MV cations are located. The low-temperature α phase was also refined in the polar space group $P2_1$, suggesting an isostructural monoclinic-monoclinic (Cc-Cc) phase transition. The differences between α and β phases are summarized in

Fig. S4 and Table S1 in the Supplemental Material [35]. It is noteworthy that, in most hybrid ferroelectrics, the contribution of the polar organic cations to the polarization of the crystal remains ambiguous. However, in (MV) [SbI$_5$], the MV cation has a symmetric configuration, and the two adjacent [SbI$_5$] chains adopt the transconnected mode. This arrangement results in the polarization of the crystal being primarily determined by the distortion of halometal octahedral chains and the movement of organic cations along the b axis, as shown in the Figs. 1(b) and 1(c). When focusing solely on the [SbI$_5$] chains, the dipoles are noncollinear due to the movement of iodine atoms in neighboring chains. A similar connecting mode has been reported in α-phase (MV) [BiBr$_5$] [36]. It is crucial to emphasize that the movement of the MV cations along the b axis also contributes to the polarization. A detailed analysis can be found in the Supplemental Material [35].

The ferroelectric property of (MV) [SbI$_5$] is confirmed by the observation of a typical polarization-electric field (P-E) hysteresis loop, as shown in Fig. 1(e). At room temperature,

the spontaneous polarization (P_s) and coercive field along the *b* axis (polar axis) are ~4 μC/cm² and ~0.25 kV/cm, respectively, at a frequency of 10 Hz. The value of P_s has been further validated through the positive-up negative-down measurements (Fig. S7(a) in the Supplemental Material [35]). The P_s value is comparable with those of other hybrid ferroelectrics, such as (trimethylchloromethylammonium)CdBr$_3$ (TMCM-CdBr$_3$: 3.5 μC/cm^2) [37], hexane-1,6-diammonium pentaiodobismuth (HDA-BiI$_5$: 6.2 μC/cm^2) [21], (3-pyrrolinium) CdBr$_3$ (~7 μC/cm^2) [38], C$_6$H$_5$N(CH$_3$)$_3$CdCl$_3$ [(PTMA) CdCl$_3$: ~3.5 μC/cm^2] [39], and the coercive field is comparable with that of (MV) [BiI$_3$Cl$_2$] (0.1–0.2 kV/cm) [29] and NaKC$_4$H$_4$O$_6$ · 4H$_2$O (Rochelle salt; 0.07–0.1 kV/cm) [40], much lower than most hybrid ferroelectrics.

B. Electronic structure of (MV) [SbI$_5$]

The black color of the crystal (Fig. S1 in the Supplemental Material [35]) suggests strong light absorption, making (MV) [SbI$_5$] potentially advantageous for investigating the BPVE. Interestingly, UV-vis-NIR absorption spectra obtained at room temperature [Fig. 1(d)] reveals two absorption edges at ~800 and 1000 nm. Using the Tauc plot method [41], we obtained direct band gap values of 1.47 and 1.96 eV, respectively. Such a narrow band gap is expected to enhance photocarrier generation and lead to enhanced photovoltaic response.

To better understand the electronic structure of (MV) [SbI$_5$], the energy band and corresponding density of states (DOS) were calculated. As shown in Fig. 1(f), a rather flat band (labeled as CBM1) gives rise to a direct band gap of 1.42 eV, and another gap of 1.98 eV (corresponding to the energy band contributed by the [SbI$_5$] inorganic frameworks, labeled as CBM2) is also revealed; both are close to the experimentally observed values. The partial DOS (PDOS) [Figs. 1(g) and 1(h)] indicates that the VBM originates mainly from the Sb 5*s* states and I 5*p* states, which are the same as that of most hybrid materials. Unexpectedly, as shown in Fig. 1(g), the two flat bands between 1.4 and 1.7 eV are dominated by C 2*p* states, H 2*s* states, and N 2*p* states from the MV^{2+} group. Note that the I 5*p* also has a small contribution to the conduction band minimum (CBM), suggesting a relatively strong interaction between organic cations and the inorganic framework. The smaller gap of 1.42 eV allows for more photons to be absorbed and electron-hole pairs to be generated, which is accompanied by an electron transfer to the MV^{2+} groups from the inorganic framework. A similar band structure has been reported in C$_7$H$_7^+$-doped GAPbI$_3$ (GA = C(NH$_2$)$_3^+$) [42], [Ga − Tpy$_2$] PbI$_5$ (Tpy: 2,2′;6′,2″-terpyridine) [43], and in perovskite materials that incorporate the π-conjugated pyrene-containing A-site cations [28]. These materials have in common that they all contain π-conjugated organic ligands. These results suggest a strategy for developing narrow-band-gap hybrid materials by designing the A-site organic groups. For hybrid ferroelectrics, the relatively flat band indicates large effective masses of electrons and low leakage current, enabling the coexisting of switchable spontaneous polarization (*P-E* loop) and superior light absorption capability (black crystals).

C. Switchable photovoltaic effect in (MV) [SbI$_5$]

To investigate the photovoltaic characteristics of (MV) [SbI$_5$], two silver electrodes of 1800 × 400 μm separated by ~200 μm were prepared to measure the photocurrent parallel to the *b* axis. Prior to measurements, voltage pulses corresponding to an electric field of 300 V/cm along the *b* axis were applied to the device to set the polarization in the desired direction. As shown in Fig. 2(a), a laser with an intensity of 35 mW/cm^2 at 445 nm irradiates the *ab* plane of the crystal along the *c* axis, with the polarization direction of light aligned along the polar axis. Large open-circuit voltage (V_{oc}) and short-circuit current (I_{sc}) of −2.4 V and 18.2 pA, respectively, are observed for the positive polarization state, and 2.52 V/−23.8 pA for the negative polarization state. As the light intensity increases to 101 mW/cm^2, V_{oc} and I_{sc} increase to ~4.1 V and 51 pA, respectively. The above-band-gap V_{oc} and the sinusoidal dependence of photocurrent on the light polarization direction (Fig. S10 in the Supplemental Material [35] for details regarding the calculation of BPVE [44,45], see Text 3 in the Supplemental Material [35]) clearly suggest the BPVE due to ferroelectricity [Figs. 2(b) and 2(c)]. Multiple switching cycles confirm the stability of the photovoltaic response [Fig. 2(d)], and the light intensity dependency under 445 nm illumination is shown in Figs. 2(e) and 2(f). The V_{oc} already exceeds the band gap under only 3 mW/cm^2. As the light intensity increases to 168 mW/cm^2, the I_{sc} value increases almost linearly, but the V_{oc} value increases rapidly initially and saturates to ~5.0 V.

D. Photovoltaic response under light of different wavelengths

To investigate the effects of the two distinct conduction band components (the flat band from the MV groups and the band from the [SbI$_5$] inorganic frameworks), single crystals of (MV) [SbI$_5$] were illuminated with 405 nm (~3.06 eV), 450 nm (~2.75 eV), 520 nm (~2.38 eV), 650 nm (~1.91 eV), 808 nm (~1.53 eV), 905 nm (~1.37 eV), and 950 nm (~1.31 eV) lasers. As show in Figs. 3(a), 3(b), and S9(a) in the Supplemental Material [35], changes in the photoconductivity are clearly seen following the photoexcitation. More interestingly, reversal of the photocurrent direction is observed when photon energy goes above 1.85 eV. This is also seen in Figs. 3(c) and S9(b) in the Supplemental Material [35], which shows the current-time response with light ON and OFF under the seven lasers. In Fig. 3(d), we show the normalized photocurrent under different laser irradiations based on light intensity. The results indicate that (MV) [SbI$_5$] can extend the photovoltaic response into the infrared region due to the flat band contributed by the MV groups. However, the opposite photocurrent directions mean that the overall performance under sunlight would be compromised. It is thus crucial that we understand the origin of the photocurrent reversal.

E. Modeling and theoretical calculations

The BPVE is commonly understood based on models of shift current and ballistic current [46–48]. Ballistic photovoltaic current arises from the asymmetric distribution of hot photocarrier momenta in reciprocal space when they relax to the bottom of the conduction band. Meanwhile, shift
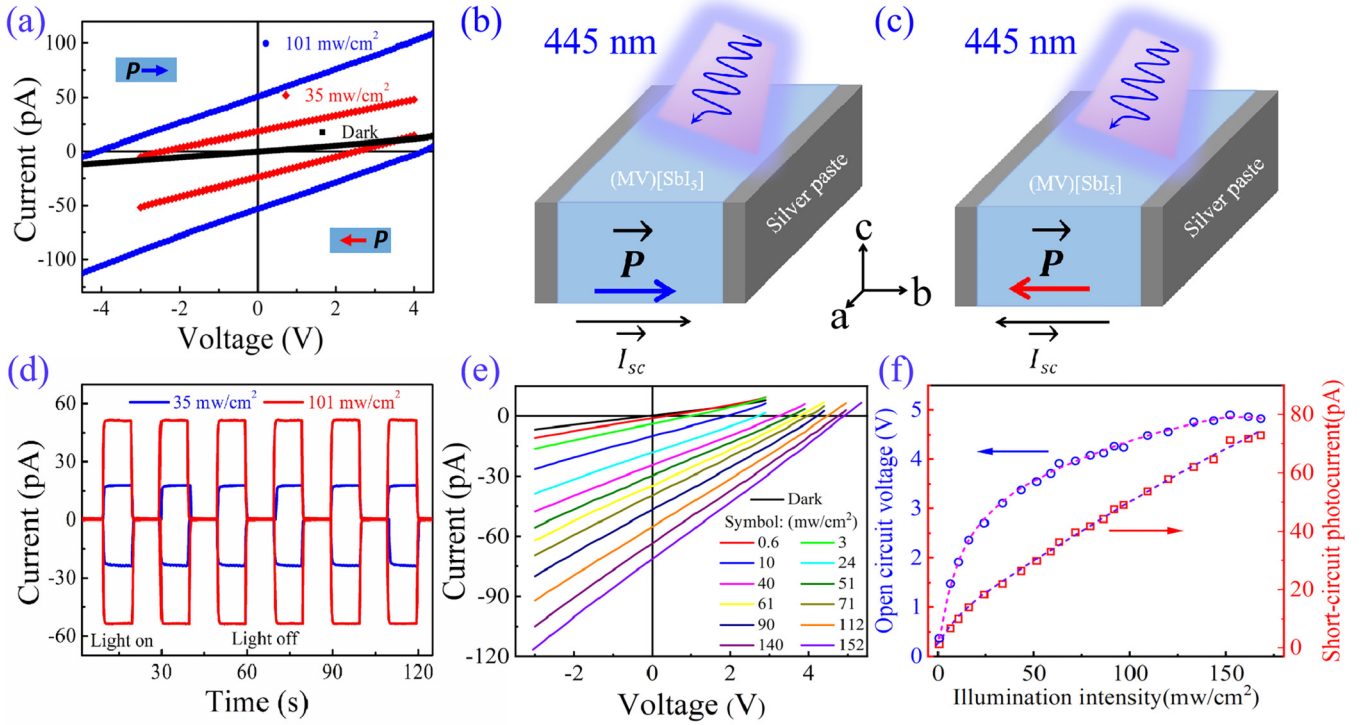
FIG. 2. (a) Photovoltaic response of (MV) [SbI$_5$]. Both directions of V_{oc} and I_{sc} can be reversed by switching the spontaneous polarization. Schematics of tunable photocurrent directions in the (b) positive and (c) negative polarization states. (d) Current-time response acquired with the illumination ON and OFF. (e) Photovoltaic response of (MV) [SbI$_5$] at different illumination intensities. (f) V_{oc} and I_{sc} as a function of illumination intensity.

current is associated with the shift of electron clouds in real space upon photon excitation. In our experiments, band-edge excitations corresponding to CBM1 contributed by the MV group (808, 905, and 950 nm lasers) and CBM2 from the inorganic framework (520 and 650 nm lasers) are investigated,
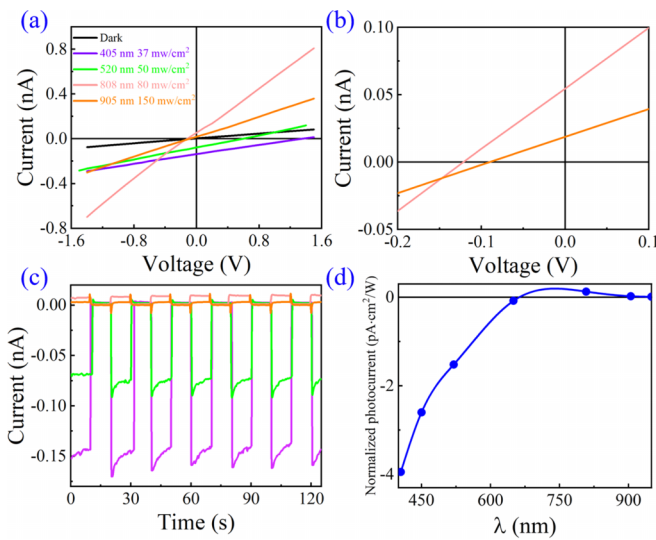

FIG. 3. (a) I-V characteristics of (MV) [SbI$_5$] upon illumination with light of different wavelengths. (b) Magnified view of the I-V characteristics of (MV) [SbI$_5$] under infrared light irradiation. (c) I-t response acquired with light ON and OFF. (d) Normalized photocurrent under light of different wavelengths.

where ballistic photocurrent is likely insignificant. We thus conducted first-principles calculations of the shift currents under these laser illuminations. Additionally, shift current generated by photoexcitations under 405, 445, and 450 nm lasers were also calculated with the contribution of ballistic currents neglected. From the band structure of (MV) [SbI$_5$], we may deduce that the reversal of photocurrent direction under illumination by different lasers is likely related to the change of electron shift pathways when they are excited to conduction band states associated with the MV groups and the [SbI$_5$] inorganic frameworks, respectively. To evaluate this hypothesis, we examined the details of electronic states at E (−0.5 0.5 0.5) and Y (−0.5 0 0) k points.

We first consider excitation to the flat band contributed by the MV cations at the Y point [Fig. 4(a)]. The corresponding charge density plots demonstrate that electrons predominantly transfer from the [SbI$_5$] chains to the MV cations. However, since the MV cations are distributed approximately symmetrically around the [SbI$_5$] chains, determining the direction of net electron transfer becomes challenging. To discern real-space electron transfer more clearly, we look into the charge density difference between the flat band and the VBM [Figs. 4(b) and 4(c)]. Connecting Sb-Sb as a reference line [Fig. 4(c)], we observed an asymmetric electron loss by Sb. Notably, more electrons are lost in the negative direction along the b axis. Consequently, the photocurrent flows in the positive direction of the b axis, opposite to the polarization. Similarly, excitations near the band edge at the E (−0.5 0.5 0.5) k point result in the same pattern (Figs. S14(a)–S14(c) in the Supplemental Material [35]). This indicates that the photocurrent
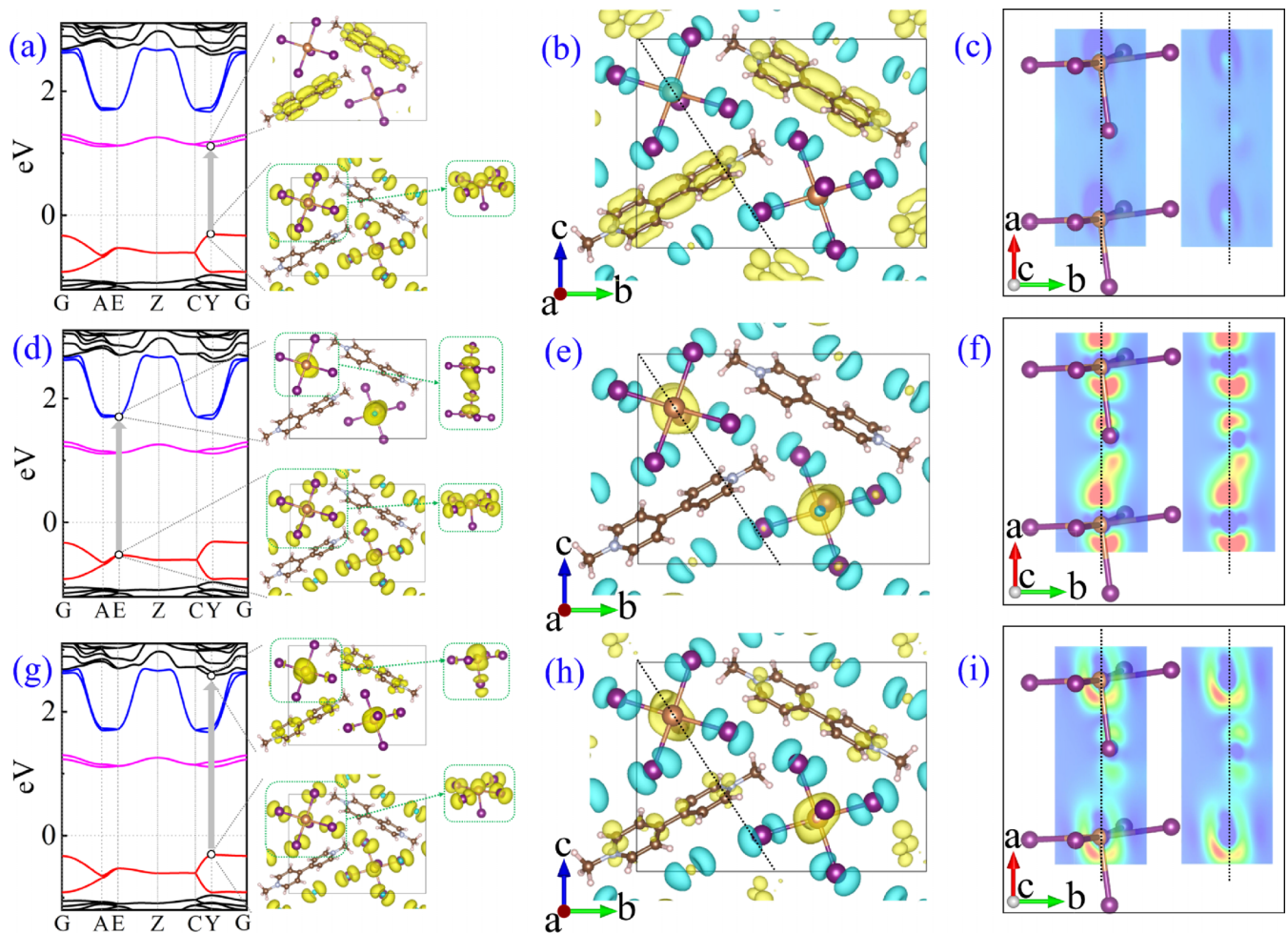
FIG. 4. (a), (d), and (g) Three pathways for electron excitation from the valence band to the conduction band; arrows represent the different transitions considered here. The insets show the charge density for the corresponding conduction bands and valence bands at E $(-0.5\ 0.5\ 0.5)$ k point and Y $(-0.5\ 0\ 0)$ k point. (b), (e), and (h) Charge density differences between the conduction band and the valence band for the three electron excitation pathways; the dashed lines represent cross-sections along the I-Sb-I direction of the same [SbI$_5$] inorganic chain. Yellow symbolizes the accumulation of electrons, while blue signifies the depletion of electrons. (c), (f), and (i) respectively depict the two-dimensional charge density differences along the cross-sections in (b), (e), and (h).

produced by excitations from the valence band to the flat band contributed by MV cations flows in the opposite direction to the polarization.

Next, we look at the excitations between 1.9 and 2.1 eV at the E point, as shown in Fig. 4(d). We observed that electrons primarily transferred from I$_{equatorial}$ in the equatorial plane of the [SbI$_5$] chains to the Sb atoms and $I_{bridging}$ bridging two Sb atoms under this excitation, resulting in photocurrent along the polarization direction. This conclusion was supported by the charge density differences depicted in Figs. 4(e) and 4(f). However, excitations at the Y $(-0.5\ 0\ 0)$ k point yields the opposite result, as shown in Figs. S14(d)–S14(f) in the Supplemental Material [35]. Here, electrons transfer from the [SbI$_5$] chains to the MV cations. Upon careful examination of the PDOS shown in Fig. 1(g), we noticed a minor contribution from the MV cations within the energy range of 1.5–2 eV. This indicates a competition between two electron pathways under excitations between red and infrared lights, generating photocurrents in opposite directions and a much-reduced net response. This explains the significantly smaller photocurrent

observed under 650 nm laser compared with that under 405, 450, and 520 nm lasers. However, excitations in the higher-energy range exhibit distinct characteristics. Examples of dominant transitions within the range of 2.8–3.6 eV are illustrated in Figs. 4(g) and S14(g) in the Supplemental Material [35]. Electrons transfer mostly from I$_{equatorial}$ of the [SbI$_5$] chains to Sb atoms and $I_{bridging}$, with a small portion moving to the MV cations. This combined effect ultimately result in shift current along the polarization direction.

In conclusion, the intensity and direction of the photocurrent depend on the electronic structure of the material. Photocurrents generated from excitations to MV cations exhibit an opposite direction to those arising from excitations to Sb and $I_{bridging}$ atoms. Under low-energy excitations, photocurrents opposing the polarization direction emerge. Under intermediate energy excitation, two competing mechanisms from different excitation pathways attenuate the magnitude of the photocurrent. Under high-energy excitations, although both mechanisms coexist within the same excitation pathway, the dominant contribution comes from electrons excited

from the valence band to Sb and $I_{bridging}$ atoms, resulting in a current along the polarization direction. These results also indicate that the BPVE in ferroelectric materials is not simply dependent on the spontaneous polarization but a shift vector describing the net displacement of electrons upon excitation, which in turn depends on the atomic displacements. In (MV) [SbI$_5$], the movement of $I_{bridging}$ in the [SbI$_5$] chain induces an asymmetric distribution of charge density between Sb and I, fundamentally influencing the shift vector during electronic excitation.

IV. DISCUSSION

We report here on the study of the BPVE in a hybrid ferroelectric (MV) [SbI$_5$] with a small band gap of 1.47 eV, which arises from a CBM formed by energy states from the MV groups. It improves light absorption significantly on one hand. On the other hand, the relative isolation of the organic groups means the band is rather flat, leading to large carrier mass and low leakage current under external electric field, which is advantageous in maintaining the ferroelectric property (switchable polarization). Further studies reveal above-band-gap V_{oc} as large as ~5 V and light polarization-dependent photocurrent, consistent with characteristics of the BPVE. Further analysis uncovers that the involvement of the MV groups in the conduction band prompts two distinct electron transfer pathways in (MV) [SbI$_5$] when excited by photons of different energies. Consequently, this gives rise to photocurrents flowing in opposite directions. In this paper, we not only demonstrate a feasible approach for obtaining hybrid ferroelectrics with small band gaps but also improve our understanding of the BPVE.

[1] A. Kitai, *Principles of Solar Cells, LEDs and Diodes: The Role of the PN Junction* (John Wiley & Sons, Chichester, 2011).

[2] M. A. Green, *Silicon Solar Cells: Advanced Principles and Practice* (Bridge Printery, Sydney, 1995).

[3] W. Shockley and H. J. Queisser, Detailed balance limit of efficiency of *p-n* junction solar cells, J. Appl. Phys. **32**, 510 (1961).

[4] NREL, Reseach Cell Efficiency Record, (2024), https://www.nrel.gov/pv/assets/pdfs/best-research-cell-efficiencies.pdf.

[5] Y. Fu, S. Jin, and X.-Y. Zhu, Stereochemical expression of ns^2 electron pairs in metal halide perovskites, Nat. Rev. Chem. **5**, 838 (2021).

[6] J. Ma and L.-W. Wang, Nanoscale charge localization induced by random orientations of organic molecules in hybrid perovskite CH$_3$NH$_3$PbI$_3$, Nano Lett. **15**, 248 (2015).

[7] B. Huang, Z. Liu, C. Wu, Y. Zhang, J. Zhao, X. Wang, and J. Li, Polar or nonpolar? That is not the question for perovskite solar cells, Natl. Sci. Rev. **8**, nwab094 (2021).

[8] K. Frohna, T. Deshpande, J. Harter, W. Peng, B. A. Barker, J. B. Neaton, S. G. Louie, O. M. Bakr, D. Hsieh, and M. Bernardi, Inversion symmetry and bulk Rashba effect in methylammonium lead iodide perovskite single crystals, Nat. Commun. **9**, 1829 (2018).

[9] Y. T. Liu, L. Collins, R. Proksch, S. Kim, B. R. Watson, B. Doughty, T. R. Calhoun, M. Ahmadi, A. V. Ievlev, S. Jesse *et al.*, Chemical nature of ferroelastic twin domains in CH$_3$NH$_3$PbI$_3$ perovskite, Nat. Mater. **17**, 1013 (2018).

[10] L. M. Garten, D. T. Moore, S. U. Nanayakkara, S. Dwaraknath, P. Schulz, J. Wands, A. Rockett, B. Newell, K. A. Persson, S. Trolier-McKinstry *et al.*, The existence and impact of persistent ferroelectric domains in MAPbI$_3$, Sci. Adv. **5**, eaas9311 (2019).

[11] T. Choi, S. Lee, Y. Choi, V. Kiryukhin, and S. W. Cheong, Switchable ferroelectric diode and photovoltaic effect in BiFeO$_3$, Science **324**, 63 (2009).

[12] M. M. Yang, D. J. Kim, and M. Alexe, Flexo-photovoltaic effect, Science **360**, 904 (2018).

[13] V. M. Fridkin, *Photoferroelectrics* (Springer-Verlag, Berlin, 2012).

[14] A. Chynoweth, Surface space-charge layers in barium titanate, Phys. Rev. **102**, 705 (1956).

[15] W. Koch, R. Munser, W. Ruppel, and P. Würfel, Bulk photovoltaic effect in BaTiO$_3$, Solid State Commun. **17**, 847 (1975).

[16] S. Han, M. F. Li, Y. Liu, W. Q. Guo, M. C. Hong, Z. H. Sun, and J. H. Luo, Tailoring of a visible-light-absorbing biaxial ferroelectric towards broadband self-driven photodetection, Nat. Commun. **12**, 284 (2021).

[17] R. Guo, L. You, Y. Zhou, Z. S. Lim, X. Zou, L. Chen, R. Ramesh, and J. L. Wang, Non-volatile memory based on the ferroelectric photovoltaic effect, Nat. Commun. **4**, 1990 (2013).

[18] L. You, F. Zheng, L. Fang, Y. Zhou, L. Z. Tan, Z. Zhang, G. H. Ma, D. Schmidt, A. Rusydi, L. Wang *et al.*, Enhancing ferroelectric photovoltaic effect by polar order engineering, Sci. Adv. **4**, eaat3438 (2018).

[19] A. Bhatnagar, A. Roy Chaudhuri, Y. Heon Kim, D. Hesse, and M. Alexe, Role of domain walls in the abnormal photovoltaic effect in BiFeO$_3$, Nat. Commun. **4**, 2835 (2013).

[20] Y. Yun, L. Mühlenbein, D. S. Knoche, A. Lotnyk, and A. Bhatnagar, Strongly enhanced and tunable photovoltaic effect in ferroelectric-paraelectric superlattices, Sci. Adv. **7**, eabe4206 (2021).

[21] H. Y. Zhang, Z. H. Wei, P. F. Li, Y. Y. Tang, W. Q. Liao, H. Y. Ye, H. Cai, and R. G. Xiong, The narrowest band gap ever observed in molecular ferroelectrics: Hexane-1, 6-diammonium pentaiodobismuth (III), Angew. Chem. **130**, 535 (2018).

[22] S. Han, X. Liu, Y. Liu, Z. Xu, Y. Li, M. Hong, J. H. Luo, and Z. H. Sun, High-temperature antiferroelectric of lead iodide hybrid perovskites, J. Am. Chem. Soc. **141**, 12470 (2019).

[23] H. Y. Zhang, X. J. Song, X. G. Chen, Z. X. Zhang, Y. M. You, Y. Y. Tang, and R. G. Xiong, Observation of vortex domains in a two-dimensional lead iodide perovskite ferroelectric, J. Am. Chem. Soc. **142**, 4925 (2020).

[24] M. K. Jana, R. Song, H. Liu, D. R. Khanal, and D. B. Mitzi, Organic-to-inorganic structural chirality transfer in a 2D hybrid perovskite and impact on Rashba-Dresselhaus spin-orbit coupling, Nat. Commun. **11**, 4699 (2020).

[25] W. Q. Liao, Y. Zhang, C. L. Hu, J. G. Mao, H. Y. Ye, P. F. Li, S. D. Huang, and R. G. Xiong, A lead-halide perovskite molecular ferroelectric semiconductor, Nat. Commun. **6**, 7338 (2015).

[26] S. S. Wang, X. T. Liu, L. N. Li, C. M. Ji, Z. H. Sun, Z. Y. Wu, M. C. Hong, and J. H. Luo, An unprecedented biaxial trilayered hybrid perovskite ferroelectric with directionally tunable photovoltaic effects, J. Am. Chem. Soc. **141**, 7693 (2019).

[27] W. J. Yin, J. H. Yang, J. Kang, Y. Yan, and S. H. Wei, Halide perovskite materials for solar cells: A theoretical review, J. Mater. Chem. A **3**, 8926 (2015).

[28] J. J. Xue, R. Wang, X. H. Chen, C. L. Yao, X. Y. Jin, K. L. Wang, W. C. Huang, T. Y. Huang, Y. P. Zhao, Y. X. Zhai *et al.*, Reconfiguring the band-edge states of photovoltaic perovskites by conjugated organic cations, Science **371**, 636 (2021).

[29] N. Leblanc, N. Mercier, L. Zorina, S. Simonov, P. Auban-Senzier, and C. Pasquier, Large spontaneous polarization and clear hysteresis loop of a room-temperature hybrid ferroelectric based on mixed-halide [BiI$_3$Cl$_2$] polar chains and methylviologen dication, J. Am. Chem. Soc. **133**, 14924 (2011).

[30] Y. Lei, S. Wang, S. Ma, Y. Shi, D. Fu, and W. Liu, Ultra-low electric field-driven dielectric tunability in hybrid ferroelectric (MV) [BiI$_3$Cl$_2$], Appl. Phys. Lett. **114**, 182902 (2019).

[31] G. Kresse and J. Furthmüller, Efficient iterative schemes for *ab initio* total-energy calculations using a plane-wave basis set, Phys. Rev. B **54**, 11169 (1996).

[32] G. Kresse and J. Furthmüller, Efficiency of *ab-initio* total energy calculations for metals and semiconductors using a plane-wave basis set, Comput. Mater. Sci. **6**, 15 (1996).

[33] D. Hamann, M. Schlüter, and C. Chiang, Norm-conserving pseudopotentials, Phys. Rev. Lett. **43**, 1494 (1979).

[34] F. Ortmann, F. Bechstedt, and W. Schmidt, Semiempirical van der Waals correction to the density functional description of solids and molecular structures, Phys. Rev. B **73**, 205101 (2006).

[35] See Supplemental Material at http://link.aps.org/supplemental/10.1103/PhysRevB.109.104110 for the XRD, DSC, AFM, and details of bulk photovoltaic effect (BPVE) calculations.

[36] W. Bi, N. Leblanc, N. Mercier, P. Auban-Senzier, and C. Pasquier, Thermally induced Bi (III) lone pair stereoactivity: Ferroelectric phase transition and semiconducting properties of (MV) BiBr$_5$ (MV = methylviologen), Chem. Mater. **21**, 4099 (2009).

[37] W. Q. Liao, Y. Y. Tang, P. F. Li, Y. M. You, and R. G. Xiong, Competitive halogen bond in the molecular ferroelectric with large piezoelectric response, J. Am. Chem. Soc. **140**, 3975 (2018).

[38] P. F. Li, W. Q. Liao, Y. Y. Tang, H. Y. Ye, Y. Zhang, and R. G. Xiong, Unprecedented ferroelectric-antiferroelectric-paraelectric phase transitions discovered in an organic-inorganic hybrid perovskite, J. Am. Chem. Soc. **139**, 8752 (2017).

[39] Y. Hu, L. You, B. Xu, T. Li, S. Morris, Y. Li, Y. Zhang, X. Wang, P. S. Lee, H. J. Fan *et al.*, Ferroelastic-switching-driven large shear strain and piezoelectricity in a hybrid ferroelectric, Nat. Mater. **20**, 612 (2021).

[40] H. Wieder, Ferroelectric polarization reversal in Rochelle salt, Phys. Rev. **110**, 29 (1958).

[41] J. Tauc, R. Grigorovici, and A. Vancu, Optical properties and electronic structure of amorphous germanium, Phys. Status Solidi B **15**, 627 (1966).

[42] G. Tang and J. Hong, Direct tuning of the band gap via electronically-active organic cations and large piezoelectric response in one-dimensional hybrid halides from first-principles, J. Mater. Chem. C **6**, 7671 (2018).

[43] Y. M. Xian, S. Y. Yuan, Y. L. Zhang, Y. X. Yuan, Y. Y. Zhang, J. D. Fan, and W. Z. Li, Electron delocalization and structure coupling promoted π-conjugated charge transport in a novel [Ga − Tpy$_2$] PbI$_5$ perovskite-like single crystal, J. Phys. Chem. Lett. **12**, 5571 (2021).

[44] V. M. Fradkin and R. M. Magomadov, Anomalous photovoltaic effect in LiNbO$_3$: Fe in polarized light, JETP Lett. **30**, 686 (1979).

[45] W. Koch, R. Munser, W. Ruppel, and P. Würfel, Anomalous photovoltage in BaTiO$_3$, Ferroelectrics **13**, 305 (1976).

[46] L. Z. Tan, F. Zheng, S. M. Young, F. Wang, S. Liu, and A. M. Rappe, Shift current bulk photovoltaic effect in polar materials—Hybrid and oxide perovskites and beyond, npj Comput. Mater. **2**, 16026 (2016).

[47] S. M. Young and A. M. Rappe, First principles calculation of the shift current photovoltaic effect in ferroelectrics, Phys. Rev. Lett. **109**, 116601 (2012).

[48] Z. Dai, A. M. Schankler, L. Gao, L. Z. Tan, and A. M. Rappe, Phonon-assisted ballistic current from first-principles calculations, Phys. Rev. Lett. **126**, 177403 (2021).